Dynamic mode decomposition of a highly confined shock-wave/boundary-layer interaction

Akshay S. Deshpande* and Jonathan Poggie†
Purdue University, West Lafayette, IN 47907-2045, USA

Shock-wave/boundary-layer interactions are highly three-dimensional and characterized by a broad range of length-and time-scales. Modal decomposition is an efficient, data-driven technique used to extract dynamically significant flow features from a time-resolved simulation. In this work, we use Sparsity-Promoting Dynamic Mode Decomposition on a shock-wave/boundary-layer interaction associated with a compression-ramp in presence of sidewalls. The ramp is inclined at an angle of 24 deg and the interaction is induced by an incoming Mach 2.25 flow. The ratio of boundary layer thickness to domain width is 0.12, which indicates a strong confinement effect of the sidewalls on the centerline flowfield. Based on the DMD modes, most of the flow energy is concentrated among the low ($St \approx O(0.01)$) and low-mid frequency modes ($St \approx O(0.1)$). The DMD modes were found to be neutral, neither amplified nor damped, suggesting that continuous disturbance input from the incoming turbulent flow is required to maintain unsteadiness in this flow. Reconstructed velocity and pressure fields corresponding to these modes confirm the presence of low-frequency shock oscillations, flapping motion of the separated shear layer, and vortex shedding from the separated zone. Additional secondary motions caused due to the presence of sidewalls were also recovered via the reconstructed modes.

$G(f)$	Power spectral density ((sig. units)^2/Hz)
L_{sep}	Separation length (m)
St	Strouhal number
T	Temperature (K)
X, Y, Z	Cartesian coordinates non–dimensionalized by $\delta_\circ$
c_{f_x}	Streamwise component of skin–friction coefficient
f	Frequency (Hz)
p	Pressure (Pa)
t	Elapsed time (s)
u	Streamwise velocity component (m/s)
v	Wall–normal velocity component (m/s)
w	Spanwise velocity component (m/s)
x, y, z	Cartesian coordinate system (m)
α	DMD mode amplitudes
$\delta_\circ$	Incoming boundary layer thickness (m)
ρ	Density (kg/m^3)
λ, μ	DMD eigenvalues
σ	RMS value of a signal (sig. units)
Superscripts:	
$'$	Fluctuating quantities
–	Mean quantities
Subscripts:	
∞	Freestream quantities
w	Wall quantities

*Graduate Research Assistant, School of Aeronautics and Astronautics, 701 W. Stadium Avenue. AIAA Student Member.
†Professor, School of Aeronautics and Astronautics, 701 W. Stadium Avenue. AIAA Associate Fellow.

I. Introduction

Shock-wave/boundary-layer interactions (SBLIs) are critical to the aerodynamic design of a high-speed vehicle. Adverse effects such as amplified aerothermal loads, increased drag, and structural fatigue decrease aircraft performance and generate significant design constraints. Researchers in this field have made significant advances in understanding the physics of this phenomenon by leveraging advanced experimental techniques and efficient computational algorithms. Detailed reviews on the past work carried out on SBLI's can be found in references [1–4]. The primary concern for aerodynamicists in this field is the low-frequency shock oscillations that cause fatigue loading on a high-speed vehicle. The frequency of these oscillations is approximately two orders of magnitude lower than the turbulence in the upstream boundary layer. Using statistical analysis, it has been observed that for interactions with attached or moderately separated flow, the shock responds to upstream fluctuations at frequencies approximately two orders of magnitude lower than that characterizing the incoming turbulence. In case of massively separated flows, downstream events such as periodic vortex shedding and breathing motion of the separated zone modulate the shock motion [4].

SBLIs in practical applications such as aircraft inlets and nozzles operating at off-design conditions deviate significantly from the two-dimensional approximation — commonly used both in experiments and computations for a tractable analysis — due to the presence of sidewalls. The influence of these additional no-slip boundaries on the flowfield has been studied both experimentally [5–11] and computationally [12–16]. In both the cases, two distinct separation regions: at the centerline and sidewall junctures were observed. The onset of three-dimensional behaviour is dictacted by the confinement ratio, δ^*/w where δ^* is the boundary layer displacement thickness in the center of the tunnel and w is the tunnel width [7]. Based on the confinement ratio, the dynamics of the centerline and corner separations are either independent or coupled. Additionally, the low-frequency shock motion observed in quasi two-dimensional cases was not affected by the presence of sidewalls.

In this study, Dynamic Mode Decomposition (DMD) [17, 18] is used to analyze the flowfield generated by a compression-ramp in the presence of sidewalls. DMD is a process which finds the best linear operator that acts as a map between two flowfields at different instances in time. The eigenvalues and eigenvectors of this linear operator are used to compute the DMD modes. The resulting modes obtained from this technique occur as complex conjugates. Each mode is associated with a discrete value of frequency, which occurs as the imaginary part of the eigenvalue. This technique has been successfully used, for example, to analyze the unsteadiness in SBLIs by Grilli et al. [19], Nichols et al. [20], Pirozzoli et al. [21], Pasquariello et al. [22], and Statnikov et al. [23]. The results presented in this study serve as an extension of the work of Deshpande and Poggie [24], who performed statistical analysis on the dataset obtained by Poggie and Porter [16], corresponding to a compression-ramp with sidewalls.

II. Methodology

In order to determine the modes that have a significant influence on the flowfield, the Sparisity-Promoting DMD (SPDMD) algorithm formulated by Jovanović et al. [25] is used. A brief description of the procedure is described in this section. The snapshots of data are arranged such that each column of the matrix corresponds to the flowfield at a particular instant in time, as shown below,

$$\begin{aligned} X &= [x(t_1) \quad x(t_2) \ \cdots \ x(t_m)] \in \mathcal{R}^{n\times m} \\ Y &= [x(t_2) \quad x(t_2) \ \cdots \ x(t_{m+1})] \in \mathcal{R}^{n\times m} \end{aligned} \tag{1}$$

where n and m are the number of data-points and snapshots, respectively. The relationship between flowfields at instants with a constant time displacement is approximated by a linear operator A as follows,

$$Y = AX \implies A = YX^{+} \tag{2}$$

where X^{+} denotes the Moore-Penrose pseudo-inverse of the matrix X. The DMD eigenvalues and modes are determined from the eigendecomposition of matrix A. A low-rank approximation for the matrix A is obtained by performing reduced SVD (Singular Value Decomposition) on X, i.e. $X = U\Sigma V^T$, where the superscript T denotes the transpose. This approximation is represented as follows,

$$\tilde{A} = U^T A U \tag{3}$$

which can be interpreted as the projection of A onto the implicit POD basis contained in U. Substituting $A = YX^{+}$ and $X^{+} = V\Sigma^{-1}U^T$ in the above equation, the approximation for the linear operator reduces to,

$$\tilde{A} = U^T Y V \Sigma^{-1} \in \mathcal{R}^{r\times r} \tag{4}$$

where r is the rank of $\tilde{A}$. The i^{th} DMD mode $\psi_i \in C^n$ following the eigendecomposition of $\tilde{A}$, i.e. $\tilde{A}\phi_i = \lambda_i\phi_i$ is calculated as,

$$\psi_i = U\phi_i \tag{5}$$

where $\phi_i \in C^n$, μ_i are the i^{th} eigenvector and eigenvalue of $\tilde{A}$, respectively. The numerical snapshots $x(t) \equiv x_t$ can be expressed as a linear combination of DMD modes in the r-dimensional subspace as,

$$x_t \approx \psi_t = \sum_{i=1}^{r} \phi_i \lambda_i^t \alpha_i, \quad t = k\Delta t;\ k \in \{0, 1, \cdots, m-1\} \tag{6}$$

and in matrix form as,

$$X \approx \underbrace{\begin{bmatrix}\psi_0 & \psi_1 & \cdots & \psi_r\end{bmatrix}}_{\Psi} = \underbrace{\begin{bmatrix}\phi_0 & \phi_1 & \cdots & \phi_r\end{bmatrix}}_{\Phi} \underbrace{\begin{bmatrix}\alpha_1 & & & \\ & \alpha_2 & & \\ & & \ddots & \\ & & & \alpha_r\end{bmatrix}}_{D_\alpha} \underbrace{\begin{bmatrix}1 & \lambda_1 & \cdots & \lambda_1^m \\ 1 & \lambda_2 & \cdots & \lambda_2^m \\ \vdots & \vdots & \ddots & \vdots \\ 1 & \lambda_r & \cdots & \lambda_r^m\end{bmatrix}}_{V_{and}} \tag{7}$$

In the equation above, D_α is a diagonal matrix of the modal amplitudes, which are indicative of the influence of a mode on the approximation of a flowfield as given by the expression in Eq. (6). The Vandermonde matrix V_{and} consists of r complex eigenvalues of $\tilde{A}$ that determine the temporal evolution of the modes and encode their frequency and growth/decay rates. For each mode, they are obtained by examining the imaginary and real component of λ_j, where

$$\mu_j = \frac{1}{\Delta t}\log(\lambda_j), \quad j = 1, r \tag{8}$$

The unknown amplitudes $\alpha_i;\ i = 1, r$ are determined by solving the following optimization problem,

$$\underset{\alpha}{\text{minimize}}\ ||X - \Phi D_\alpha V_{and}||_F^2 \tag{9}$$

where $||.||_F$ denotes the Frobenius norm and the resulting amplitudes $\alpha_{i,opt}$ optimally approximate the entire dataset. In order to determine the optimal subset of the DMD modes, the SPDMD algorithm entails solving a convex optimization problem by inducing sparsity via a penalty term, which is the l_1 norm of the vector α_i. The corresponding expression is shown in the equation below,

$$\underset{\alpha}{\text{minimize}} ||X - \Phi D_\alpha V_{and}||_F^2 + \gamma \sum_{i=1}^{r} |\alpha_i| \tag{10}$$

where γ is a positive regularization parameter. Larger values of γ encourage sparser solutions from Eq. (10), while for $\gamma = 0$, the conventional optimization problem in Eq. (9) is recovered. This procedure is carried out on the dataset obtained from the high-fidelity computations carried out by Poggie and Porter [16]. The freestream conditions are given in Table 1.

Table 1 Flow conditions.

Parameter	Value
U_∞	588 m/s
M_∞	2.25
ρ_∞	0.49 kg/m^3
T_∞	170 K
T_w	323 K
$\rho_\infty u_\infty/\mu_\infty$	25×10^6 m^{-1}

The streamwise and the wall-normal extent computational domain are $X = x/\delta_\circ = 130$ and $Z = z/\delta_\circ = 20$ respectively. The wall-normal extent varies from $Y = y/\delta_\circ = 25.4$ at the start of the domain to $Y = y/\delta_\circ = 45.1$ at its

end. The grid used for computations consisted of $4711 \times 1402 \times 1401$ points in the x, y, and z directions respectively, with a total of 9.4×10^9 points. The wall spacing in the wall-normal and spanwise directions are maintained at $\Delta y^+, \Delta z^+ = 0.51$. The grid was gradually stretched away from the floor and sidewalls towards the top boundary and center of the domain. At the inlet, a boundary-layer profile corresponding to the laminar-flow similarity solution for Mach 2.25 flow was imposed. The flow properties were extrapolated at the end and top of the domain. Transition to turbulence was achieved by tripping the boundary layer via an artificial body-force directed upstream. The mathematical expressions for implementation of the artificial trip model as well as details of numerical setup can be found in Poggie and Porter [16].

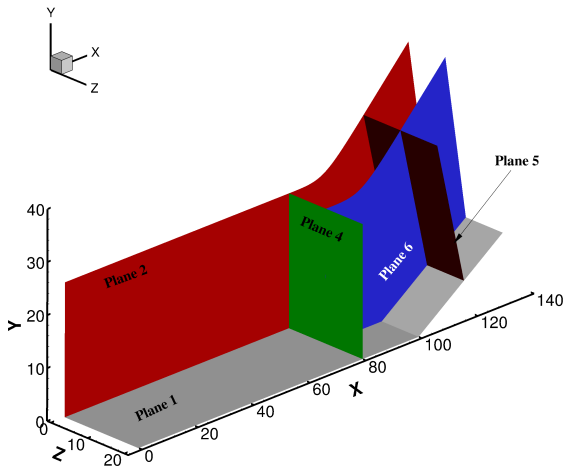

Fig. 1 Sampled planes.

The computations were run for an overall simulation time of $U_\infty t/\delta_0 = 1195$ (2.39×10^5 iterations) with a non-dimensional time step of $U_\infty t/\delta_0 = 5 \times 10^{-3}$. The calculation was initially run for about two flow-through times to establish a statistically steady state. The flow data were then saved for about seven flow-through times. The data were extracted at six different planes (see Fig. 1): the three no-slip walls (Planes 1–3), the $X = 80$ plane (Plane 4), the ramp-normal plane at $X \approx 116$ (Plane 5), and the portion of the centerplane ($Z = 10$) downstream of $X = 80$ (Plane 6). These planes were saved every 200 iterations which resulted in a total of 908 snapshots.

III. Results and Discussion

This section presents the dynamics of dominant modes obtained from the SPDMD process on five planes mentioned in Sec. II: wall (Plane 1), sidewalls (Planes 2 and 3), ramp-normal plane (Plane 5), and centerplane (Plane 6). The primitive variables used to construct the data matrix are specified for each case. The results for each of these cases are elaborated in different subsections. The mean and instantaneous flowfields, as well as the details of spectral analysis are presented in Ref. [24], and hence only select results are included here in order to orient the reader. Typically, SBLI's are characterized by low-frequency oscillations of the shock and breathing of separation bubble, low-mid frequency flapping of the separated zone, and high-frequency vortex shedding. The dominant modes corresponding to representative frequencies from each of these bins are analyzed individually for each plane.

The subset of dynamically significant modes extracted by the SPDMD algorithm was chosen such that it captured frequencies within all the three bands. For a particular mode, only the oscillatory part is reconstructed by following the process described in Nichols et al. [20] and Pasquariello et al. [22]. For a non-linear statistically stationary system, the growth rate tends to zero in the limit of infinitely many snapshots [21]. Therefore, the effect of the oscillatory part of a DMD mode on the mean flowfield can be determined using the expression shown in Eq. (11),

$$f(\mathbf{x}, t) = \overline{f}(\mathbf{x}) + a_f \, \mathrm{Re}\left[\alpha_{i,opt} \widetilde{f_i(\mathbf{x})} \exp\left(j\omega_i t\right)\right] \tag{11}$$

where a_f is a suitable amplification factor, $\overline{f}(\mathbf{x})$, $\widetilde{f_i}(\mathbf{x})$ represent the mean and the i^{th} spatial mode respectively, and ω_i is the associated frequency. The oscillatory modes mentioned previously appear in complex conjugate pairs. Hence the

contribution of the complex conjugate portion of a particular oscillatory mode is incorporated in the amplification factor a_f. The reconstructed modes were evaluated at discrete time values: $t_k = k\pi/16;\ k = 0, 1, \cdots, 31$. The corresponding animations are available on our group's website.* The chosen time-step of $\pi/16$ ensured sufficient time resolution.

A. Centerplane

Mean non-dimensional density contours (ρ/ρ_∞) on the centerplane and spectra highlighting the dominant time-scales are presented in Fig. 2. The flowfield in Figure 2(a) is analogous to a quasi-two dimensional SBLI, wherein the compression-ramp shock in the freestream bifurcates into a λ-shock foot close to the wall due to boundary layer separation. The separated zone that occurs between the two shock feet is of the "open" type, wherein the fluid is swept away from the mid-span instead of recirculating upstream as in the infinite span case. Figure 2(b) shows the spectra of compression-ramp shock location history and mass history of the separation bubble in premultipled coordinates. The former peaks in the low-frequency range at $St \approx 0.04$ and the latter peaks in the low-mid frequency range at $St \approx 0.12$.

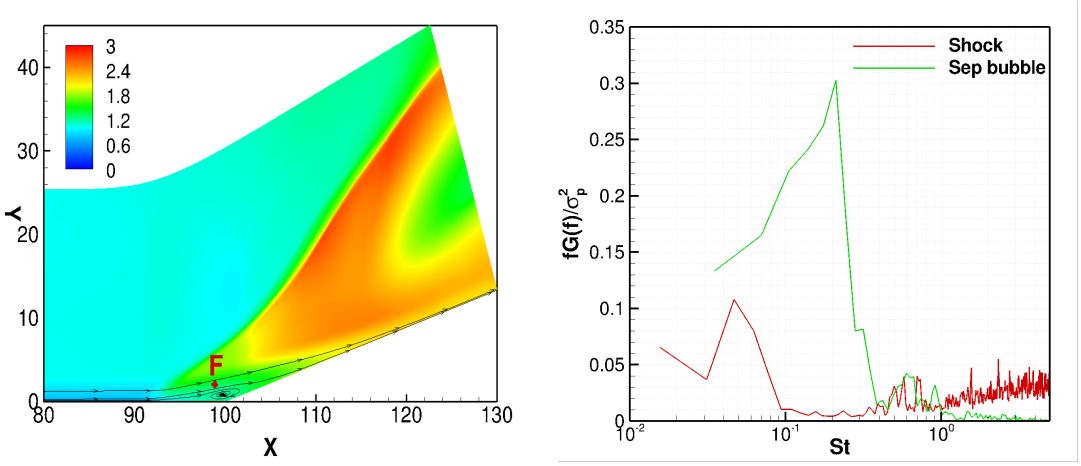

(a) Mean density contours

(b) Spectra of shock location and sep. bubble mass

Fig. 2 Flowfield characteristics on the centerplane.

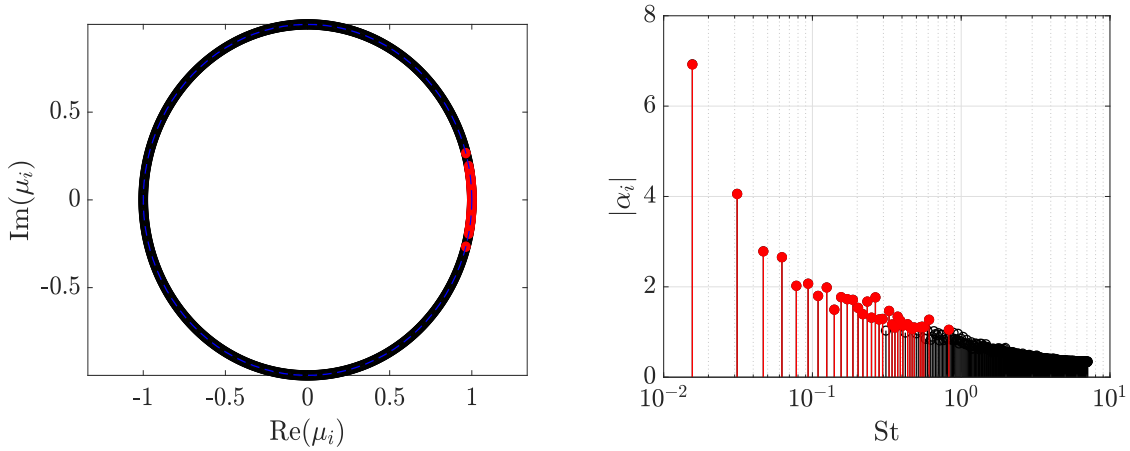

(a) Eigenspectrum

(b) Mode amplitudes

Fig. 3 DMD modes on the centerplane. Red markers indicate dominant modes obtained from SPDMD.

*See https://engineering.purdue.edu/~jpoggie/sidewalls/index.html

For this case, the data matrix used to perform SPDMD was: $\{\rho', u', v'\}^T$. Due to memory constraints, the domain size was reduced by skipping points in steps of 10 points in the streamwise direction and 5 points in the wall-normal direction, resulting in a total of $3 \times 238 \times 281$ data points. The eigenspectrum as well as the mode amplitudes are shown in Fig. 3. In Fig. 3(a), all the eigenvalues lie on the unit circle suggesting that the corresponding modes are neutral, i.e. neither damped nor amplified. Such a flow is receptive to forcing (via external disturbances or internal non-linear mechanisms) corresponding to the weakly damped global mode, thus displaying both amplifier and oscillator characteristics, as demonstrated by Poggie [26]. The optimal mode amplitudes are shown in Fig. 3(b) on the y-axis. The Strouhal number is shown on the x-axis in a log scale. The red markers in both these figures indicate the dynamically significant modes as determined from the SPDMD algorithm. The size of this subset is $N_z = 68$, with the maximum frequency of $St \approx 0.83$. The modal amplitudes decrease monotonically with increasing Strouhal numbers, with the dominant modes lying in the low and low-mid frequency range. Based on the spectra in Fig. 2(b) and the plot of mode amplitudes shown previously in Fig. 3(b), choices of representative frequencies from the low and low-mid frequency bands are $St = 0.03$ and $St = 0.12$ respectively. In case of the mid-frequency band, a value of $St = 0.6$ was chosen due its relatively higher amplitude amongst other frequencies in the same band. These values are kept consistent in all the following subsections for simultaneous interpretation of results.

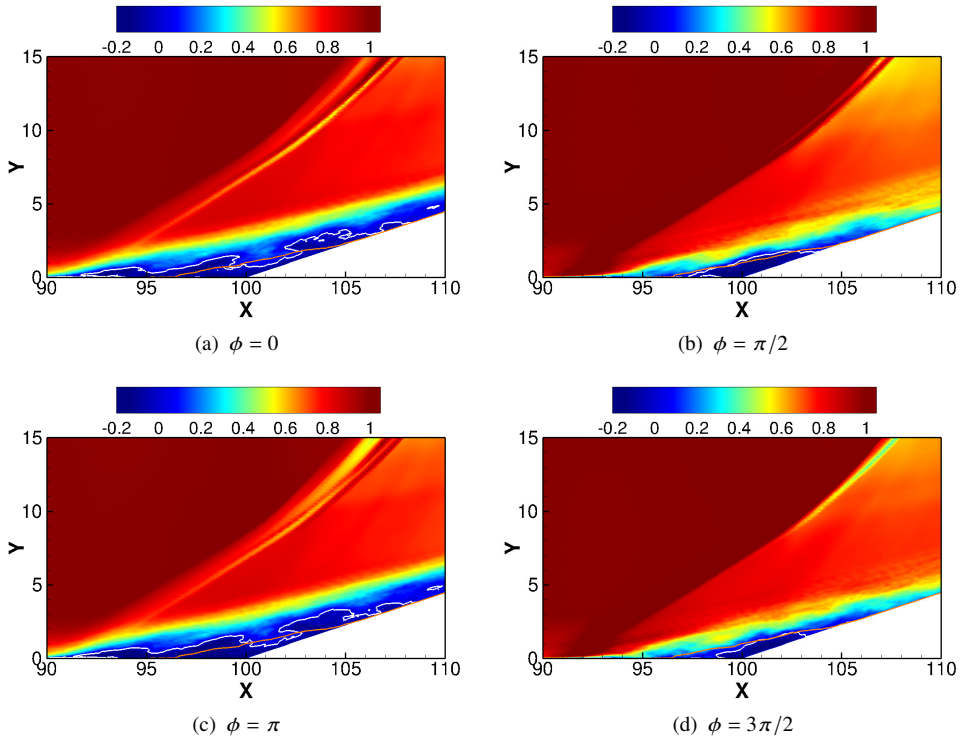

(a) $\phi = 0$ (b) $\phi = \pi/2$

(c) $\phi = \pi$ (d) $\phi = 3\pi/2$

Fig. 4 Contours of $\hat{u}/U_\infty$ describing the low-frequency breathing of the separated zone and oscillations of the compression-ramp shock. Orange and white solid lines represent the mean and instantaneous mean dividing streamline ($\hat{u}/U_\infty = 0$).

Figure 4 shows four instances of the low-frequency mode at $St = 0.03$ for equidistant phase angles: $\phi = 0, \pi/2, \pi$, and $3\pi/2$ via the contours of $\hat{u}/U_\infty$. The superscript $\widehat{\ }$ denotes a reconstructed mode. In this figure, boundary of the separated zone is differentiated using the dividing streamline ($\hat{u}/U_\infty = 0$). Mean and instantaneous locations of the same are highlighted using orange and white solid lines respectively. Starting from $\phi = 0$ in Fig. 4(a), the overall extent of the instantaneous separated zone is larger than its mean counterpart, indicating the bubble expansion phase. The compression-ramp shock – which can be identified as a region of low values of $\hat{u}/U_\infty$ – is at its most upstream location.

At $\phi = \pi/2$ in Fig. 4(b), the boundary of the instantaneous separated zone lies approximately on the mean dividing streamline. Concurrently, the compression-ramp shock translates in the downstream direction. Figure 4(c) shows the contour plot at $\phi = \pi$, wherein the instantaneous separated zone expands again, most likely following a contraction phase in $\pi/2 < \phi < \pi$. Notice that the compression-ramp shock translates upstream at this instant. The contraction

phase of the breathing motion can be visualized in Fig. 4(d) at $\phi = 3\pi/4$, as indicated by shrinking of the instantaneous separated zone below its mean and downstream movement of the compression-ramp shock. This behaviour is consistent with the observations of Nichols et al. [20] and Pasquariello et al. [22] for the low-frequency mode. The dynamics of other DMD modes at low-frequencies exhibit similar breathing motion of the separated zone and streamwise oscillations of the shock.

The dynamics of the mode at low-mid frequency ($St = 0.12$) are shown in Fig. 5. Four instances of this mode are shown for phase angles $\phi = 0, \pi/2, \pi$, and $3\pi/2$. This frequency is typically associated with the flapping motion of the shear layer/separated zone. In order to highlight the same, mean and instantaneous contour levels of $\hat{u}/U_\infty \in [0.3, 0.6]$ which lie within the shear layer are used. For the purpose of analysis, the shear layer is divided into the aft portion, which lies upstream of the ramp corner (at $X = 100$) and the rear portion, which lies downstream of it.

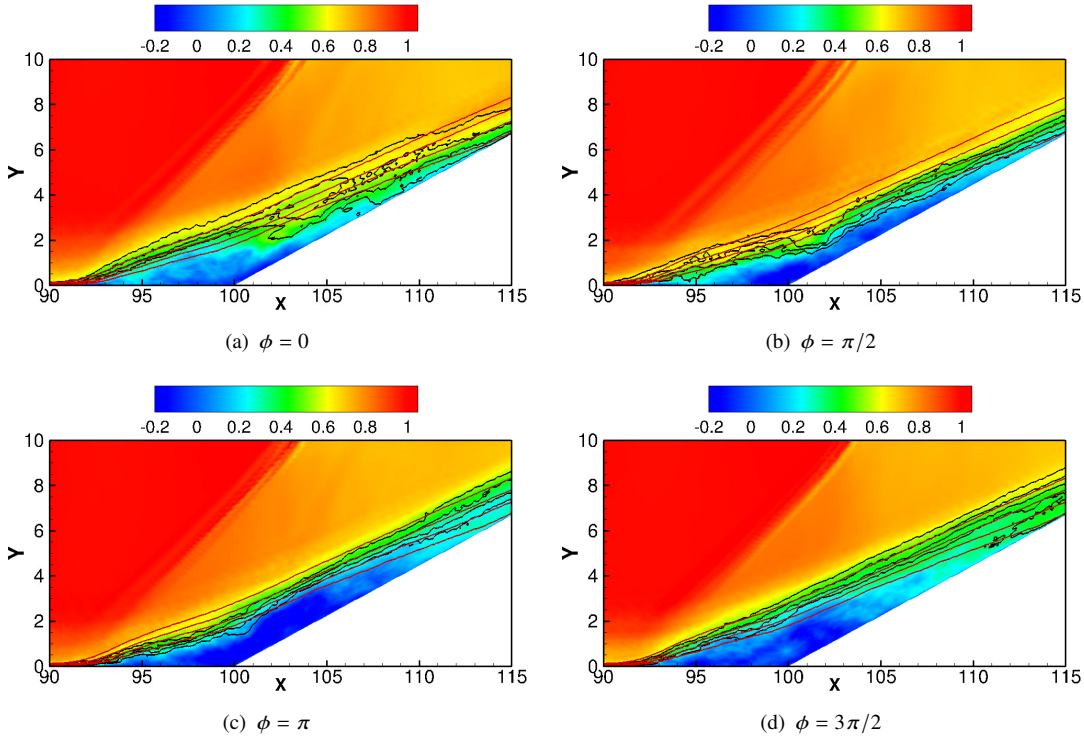

(a) $\phi = 0$ (b) $\phi = \pi/2$

(c) $\phi = \pi$ (d) $\phi = 3\pi/2$

Fig. 5 Contours of $\hat{u}/U_\infty$ depicting the low-mid frequency flapping of the separated zone. Red and black solid lines represent the mean and instantaneous contour levels of $\hat{u}/U_\infty = 0.3, 0.4, 0.5$, and 0.6.

In Fig. 5(a) at $\phi = 0$, the overall aft portion of the shear layer lies above its mean location while the rear portion lies below it. This seems to correlate with the size of the instantaneous separated zone and may represent the entrainment of low-momentum fluid into the aft portion of the shear layer. This is followed by a downward movement of the same at $\phi = \pi/2$ in Fig. 5(b). At the same instant, the rear portion is at its lowermost position and begins its upward movement. Note the increased separation extent downstream of the ramp corner as compared to Fig. 5(a). In Fig. 5(c), the aft portion of the shear layer continues its downward movement. As the separation extent downstream of the ramp corner continues to increase, the rear portion of the shear layer moves upwards. This phase most likely represents the re-injection of fluid into the separated zone. The aft portion of the shear layer begins its upward movement at $\phi = 3\pi/2$ in Fig. 5(d), while the rear portion starts moving below its mean position. Based on the description, this frequency does represent the flapping motion of the separated zone. A similar phenomenon was also observed by Statnikov et al. [23].

The flapping motion is asymmetric in nature and seems to conform to the hypothesis proposed by Eaton and Johnston [27], which attributes the same to an instantaneous imbalance between the re-injection of fluid in the separated zone and entrainment of fluid by the shear layer. Additionally in Fig. 2(b), the spectrum of the mass-history of the instantaneous separated zone peaks at $St \approx 0.12$. Since the flowfield is highly three-dimensional with an open separation (as indicated by the focus point F in Fig. 2(a)), spanwise transport of fluid away from the centerline may also contribute towards the observed flapping motion.

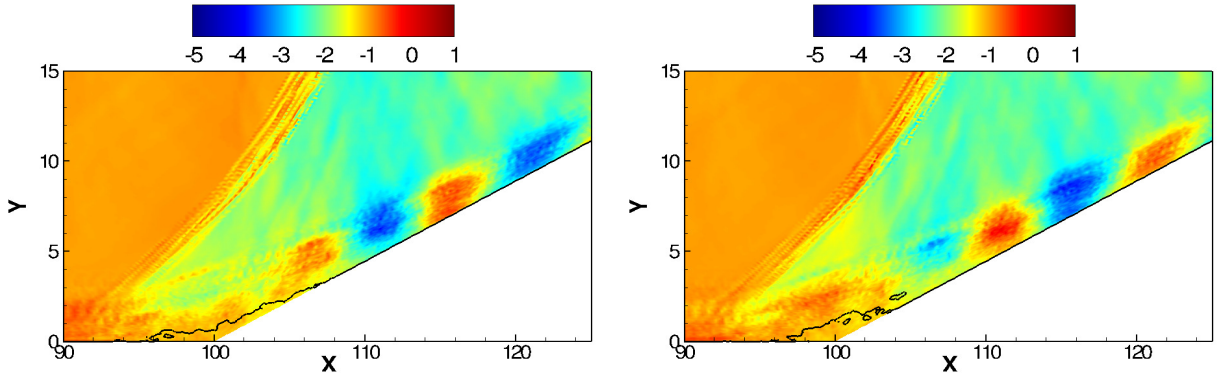

(a) $\phi = 0$ (b) $\phi = \pi$

Fig. 6 Contours of $\widehat{\rho'}/\rho_\infty$ showing the mid-frequency vortex shedding. The black solid line represents the instantaneous dividing streamline ($\hat{u}/U_\infty = 0$).

For the final frequency component, we study the dynamics associated with the mode corresponding to $St = 0.6$ in Fig. 6 by examining the contours of $\widehat{\rho'}/\rho_\infty$. This frequency typically represents vortex shedding from the separated zone. The mean is not added while reconstructing the mode in order to view the vortical structures as density perturbations. Only two phases: $\phi = 0, \pi$ of the reconstructed mode are shown. The instantaneous dividing streamline is shown as a black solid line in order to examine the effect of vortex shedding on the instantaneous reattachment location. Alternating regions of positive and negative density perturbations on the ramp are observed in the figure. In Fig. 6(a) at $\phi = 0$, a region of $\widehat{\rho'}/\rho_\infty > 0$ is present immediately downstream of reattachment. This is substituted by a region of $\widehat{\rho'}/\rho_\infty < 0$ at $\phi = \pi$, suggesting the presence of a vortical structure. The separation extent is smaller as compared to the one in Fig. 6(a). Therefore it seems that the instantaneous reattachment location moves upstream after the shedding process and downstream before it begins.

B. Ramp-normal plane

This section discusses the characteristics of DMD modes on the ramp-normal plane. We start by examining the mean density contours shown in Fig. 7(a). The sidewalls are characterized by λ-shock structures generated by the bifurcation of the compression-ramp shock, labelled as CS. The separation and reattachment shock are labelled as SS and RS respectively. The right-sidewall separation vortex is highlighted via the streamlines. Farther downstream, the λ-shock structures undergo shock reflection, resulting in a complex wave pattern. From the spectral analysis carried out by Deshpande and Poggie [24], the λ-shock structures undergo low-frequency oscillations at $St = 0.03$ (see Fig. 5 in that reference). Regions of high spectral energy density at $St = 0.12$ and $St = 0.6$ were present within the separation vortex. Figure 7(b) shows a magnified view of Fig. 7(a), focused on the bottom-left corner. The corner vortex corresponding to the left-sidewall can be clearly observed. The mean flowfield is approximately symmetric across the centerline ($Z = 10$).

The data matrix for this case consisted of $\{\rho', u', w'\}^T$. The domain size was reduced by selecting every fifth point in the wall-normal and spanwise directions, resulting in a total of $3 \times 281 \times 281$ data points. The size of the subset of dynamically significant modes is $N_z = 88$, and consists of the representative frequencies used in Sec. III.A. The eigenspectrum as well as the plot of mode amplitudes are shown in Fig. 8. In Fig. 8(a), all the eigenvalues lie on the unit circle indicating neutral modes. The spectrum of mode amplitudes shown in Fig. 8(b) is similar to the one for the centerplane case in Fig. 3(b), wherein high amplitudes are biased towards lower frequencies.

Figure 9 shows the reconstructed low-frequency DMD mode of $\hat{u}/U_\infty$ at three equally spaced phase angles: $\phi = \pi/2$, π, and $3\pi/2$. In order to demonstrate the breathing process, the contour value of $\hat{u}/U_\infty \approx 0.5$ is considered the boundary of the separated zone. The mean and instantaneous counterparts are highlighted using solid white and red lines respectively. Additionally, contour lines corresponding to $\widehat{w}/U_\infty \approx -0.1, 0.1$ are highlighted using solid and dashed black lines, respectively. They are used to monitor the spanwise motion of the separation and reattachment shock feet (within the λ-shock structure; see Fig. 7(a)) for varying phase angles. At each instant, the approximate direction that is followed by a particular shock foot is indicated by an arrow in the figure.

Both the separated zones lie approximately below their mean positions at $\phi = 0$ in Fig. 9(a). Note that the

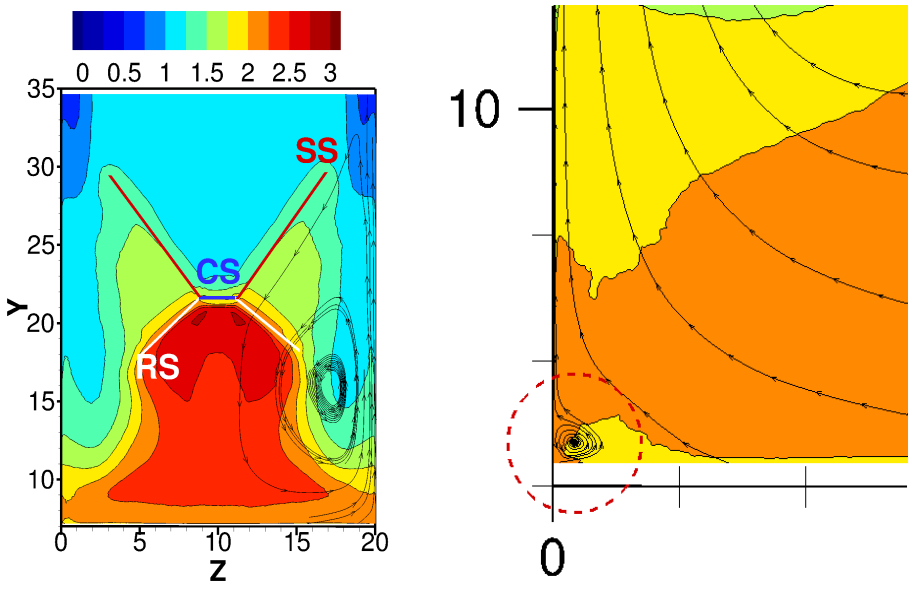

(a) Mean density contours (b) Corner vortex at the left-sidewall

Fig. 7 Mean flowfield on the ramp-normal plane.

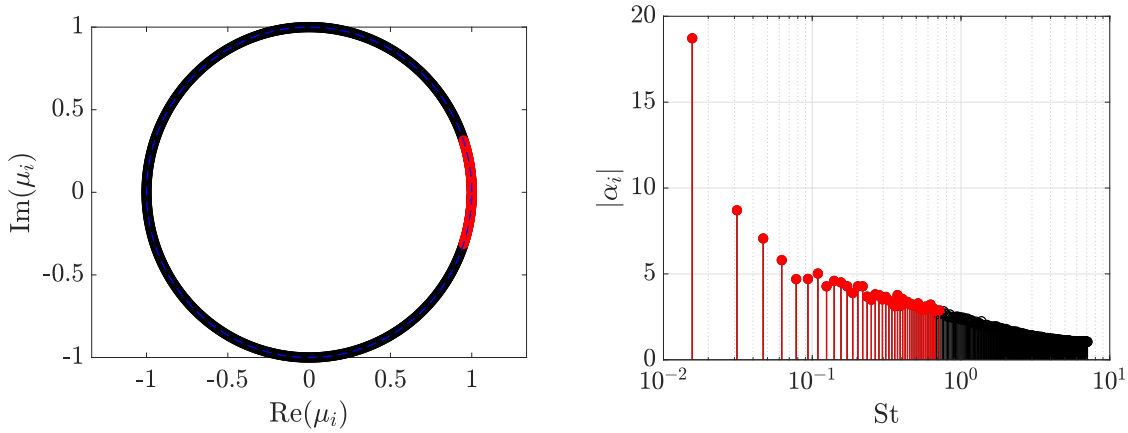

(a) Eigenspectrum (b) Mode amplitudes

Fig. 8 DMD modes on the ramp-normal plane. Red markers indicate dominant modes obtained from SPDMD.

reattachment shock-system (ensemble of shock structures post-reattachment) translates in the downstream direction at this instant, as evidenced by high magnitudes of $\hat{u}/U_\infty$ along its trace. The separation shock feet move towards the wall while the reattachment shock feet move away and towards the mid-span. In Fig. 9(b), the separated zones approach their respective mean locations at $\phi = \pi/2$ while the reattachment shock-system begins to move in the upstream direction. The angular span between the separation and reattachment shock feet increases in a forceps-like fashion due to trend reversal in spanwise velocities of the separation shock feet. At $\phi = \pi$ in Fig. 9(c), expansion of the separated zones occurs simultaneously as the reattachment shock-system translates upstream. The reattachment shock feet now move towards the wall while the separation shock feet continue moving towards the centerline. From the snapshots in this figure, the breathing of the sidewall separated zone occurs in-phase (symmetrically). An expansion of the same is concurrent with the upstream translation of the reattachment shock-system and vice-versa. Additionally, the spanwise movement of the individual λ-shock feet seem to be coupled with the low-frequency breathing motion.

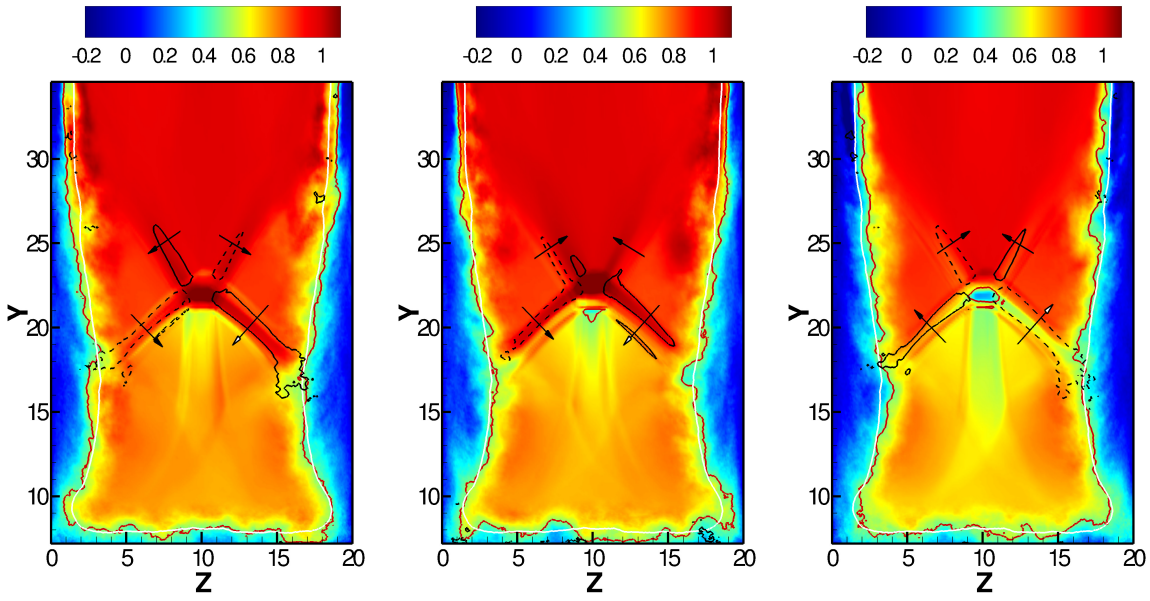

(a) $\phi = \pi/2$ (b) $\phi = \pi$ (c) $\phi = 3\pi/2$

Fig. 9 Contours of $\hat{u}/U_\infty$ describing the low-frequency breathing of the sidewall separated zones. Red and white solid lines indicate the instantaneous and mean contour levels of $\hat{u}/U_\infty = 0.5$. Solid and dashed black lines highlight instantaneous contour levels of $\widehat{w}/U_\infty = -0.1$ and 0.1 respectively.

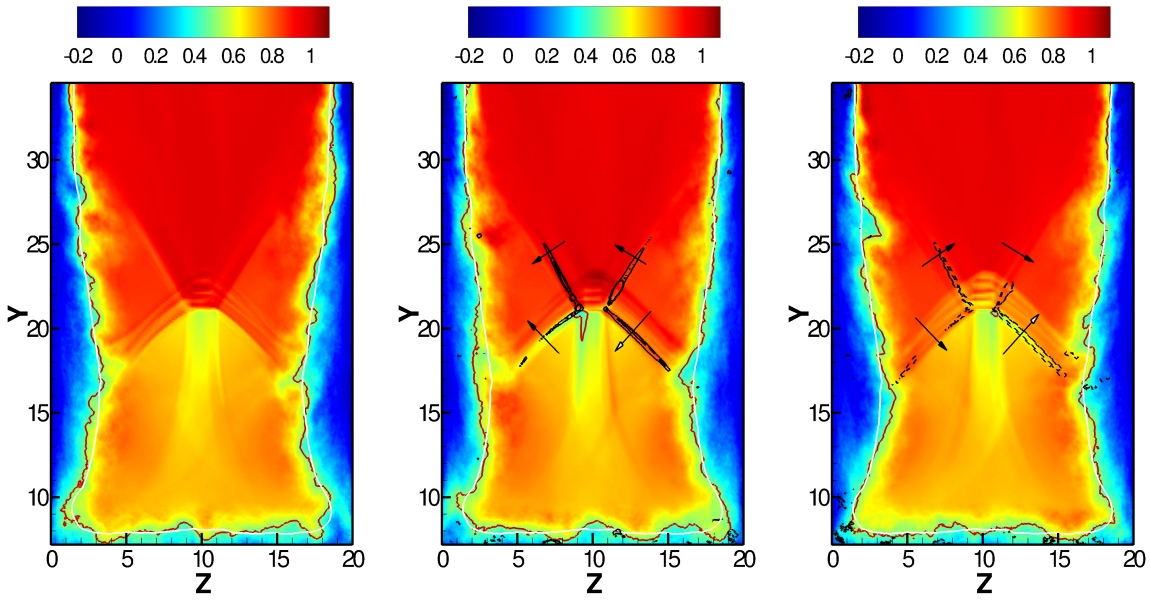

(a) $\phi = \pi/2$ (b) $\phi = \pi$ (c) $\phi = 3\pi/2$

Fig. 10 Contours of $\hat{u}/U_\infty$ describing the low-mid frequency motion the sidewall separated zones. Red and white solid lines indicate the instantaneous and mean contour levels of $\hat{u}/U_\infty = 0.5$. Solid and dashed black lines highlight instantaneous contour levels of $\widehat{w}/U_\infty = -0.08$ and 0.08 respectively.

Dynamics of the DMD mode at $St = 0.12$ are described in Figure 10 using the contours of $\hat{u}/U_\infty$. The template used in this figure is adapted from Fig. 9. In order to examine the spanwise motion of the reattachment shock-system at this

frequency, contour levels corresponding to $\widehat{w}/U_\infty = -0.08$ and 0.08 are highlighted using solid and dashed black lines respectively. Starting from $\phi = \pi/2$ in Fig. 10(a), both the separated zones lie approximately on their mean locations. At $\phi = \pi$ in Fig. 10(b), the separation size on the right-sidewall increases, while that on the left-sidewall contracts below its mean position. This causes an effective leftward movement of the core flow and the resulting asymmetry can be observed across the centerline. The angular span between the λ-shock feet on the left-sidewall decreases, while that on the right-sidewall increases. Figure 10(c) illustrates a similar phenomenon occurring at $\phi = 3\pi/2$ wherein the left-sidewall is characterized by a larger separated region while that on the right-sidewall decreases, resulting in the rightward movement of the core flow.

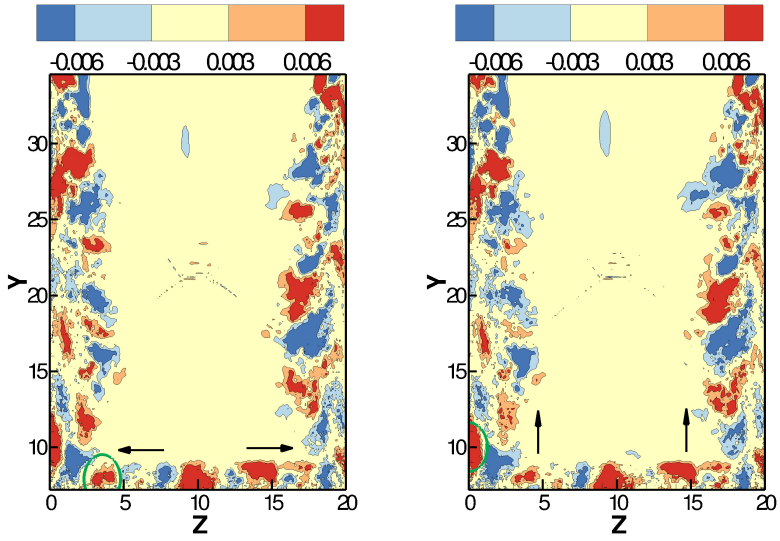

(a) $\phi = 0$ (b) $\phi = \pi$

Fig. 11 Contours of $\widehat{u'}/U_\infty$ describing the mid-frequency dynamics of the sidewall separated zones.

Contours of streamwise velocity perturbations $\widehat{u'}/U_\infty$ shown in Fig. 11 are used to study the mode associated with the mid-frequency component, $St = 0.6$. The reconstructed mode does not include contribution from the mean flowfield. Two instances of this mode are shown for phase angles, $\phi = 0$ and $\phi = \pi$ in Figs. 11(a) and 11(b), respectively. Based on these figures, the vortical structures on the floor move away from the centerline due a strong spanwise velocity component. They are then transported away from the wall, possibly by a combined influence of the sidewall separation vortex and the corner vortex (see Figs. 7(a) and 7(b)). This process can be visualized by tracking the encircled structure, which moves towards the left-sidewall at $\phi = 0$ and is swept upwards at $\phi = \pi$ as indicated by arrows in the respective figures.

C. Wall and sidewalls

This section discusses the modes on the wall and sidewalls corresponding to representative frequencies used in the previous sections. The mean pressure contours on the wall and left-sidewall are shown in Fig. 12. The contours on the right-sidewall are similar to the ones on the left, and hence are not included in the figure. The limiting streamlines as well the $c_{f_x} = 0$ contour level are included in the figure as black and white solid lines respectively.

On the floor, the shock front associated with the compression-ramp shock is curved in nature due to premature separation close to the sidewalls, as indicated by the zero skin-friction contour. The adverse pressure gradient imposed by the compression-ramp shock affects the flow at the corner more severely due to influence of two no-slip boundaries, which reduces the net momentum of the boundary layer. Across the span, the separation extent decreases away from the sidewalls, before increasing again close to the mid-span. The compression waves generated due to sidewall separated regions modify the three-dimensional shock structure, thereby moderating the pressure gradient which lowers the separation extent on the wall.

The primary and corner flows present on the wall can be determined from a critical point analysis. The flow separates at the separation node N_s and attaches along the reattachment line characterized by reattachment nodes N_a.

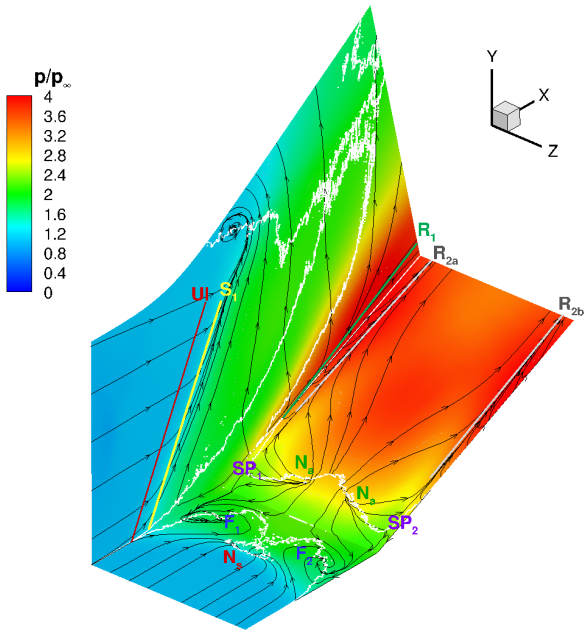

Fig. 12 Contours of mean wall pressure on the wall and left-sidewall.

The reattachment lines, R_{2a} and R_{2b} occur due to the presence of corner vortices downstream of mean reattachment (see Fig. 7(b)). Additionally, the focus points F_1 and F_2 are a source of tornado vortices which lift up fluid away from the wall in the wall-normal direction. On the left-sidewall, the incoming flow begins to turn along the upstream influence line UI and separates along S_1. Analogous to the separation on the centerplane (in Fig. 2(a)), the separated flow on the sidewall does not recirculate upstream. Instead, it follows a helical trajectory and reattaches along R_1 close to the wall. This interaction is similar to the SBLI associated with a sharp-fin, wherein the reattachment line is characterized by high aerothermal loads [28].

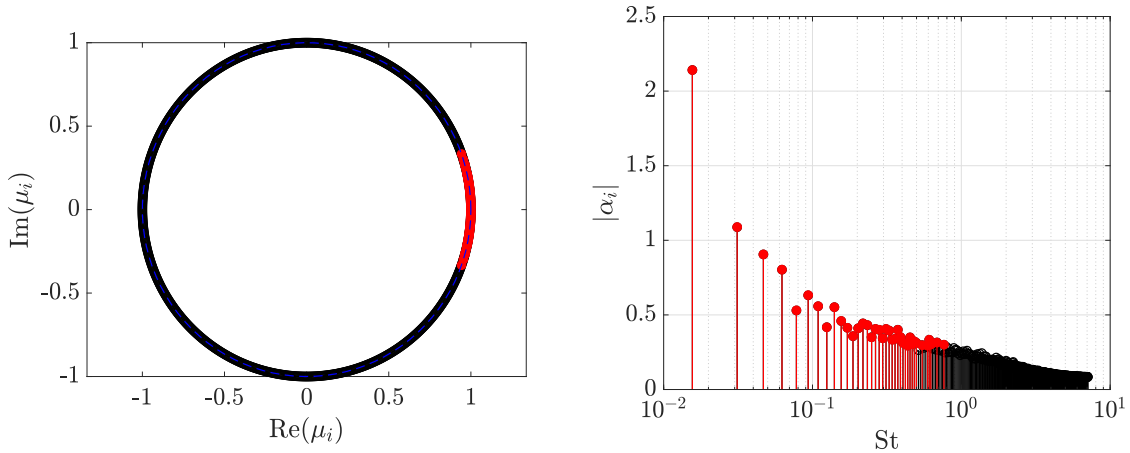

(a) Eigenspectrum

(b) Mode amplitudes

Fig. 13 DMD modes on the wall. Red markers indicate dominant modes obtained from SPDMD.

The SPDMD algorithm was applied separately on the wall and each sidewall, using a data matrix consisting of only wall pressure fluctuations. The domain size was reduced by selecting every tenth point in the streamwise direction and

every fifth point in the wall-normal and spanwise directions. Total data points on the wall and both the sidewalls were 238×281 and 281×281 respectively. The size of the subset of dynamically significant modes is $N_z = 76$ for all the cases. Since the plots of eigenspectrum and mode amplitudes obtained for all the cases were identical, they are only shown for the case of wall in Fig. 13. These plots share similar characteristics to those described in Figs. 3 and 8.

Figure 15 highlights the low-frequency motion of the compression-ramp shock as well as that of the reattachment shock-system formed downstream of mean reattachment at $St = 0.03$. The reconstructed modes are shown at four equidistant phase angles $\phi = 0, \pi/2, \pi$, and $3\pi/2$. In this figure, the mean and instantaneous levels of $\hat{p}/p_\infty = 0.2$ and 0.4 are shown using red and black solid lines respectively. The former tracks the movement of the compression-ramp shock and the latter monitors oscillations of the reattachment shock-system.

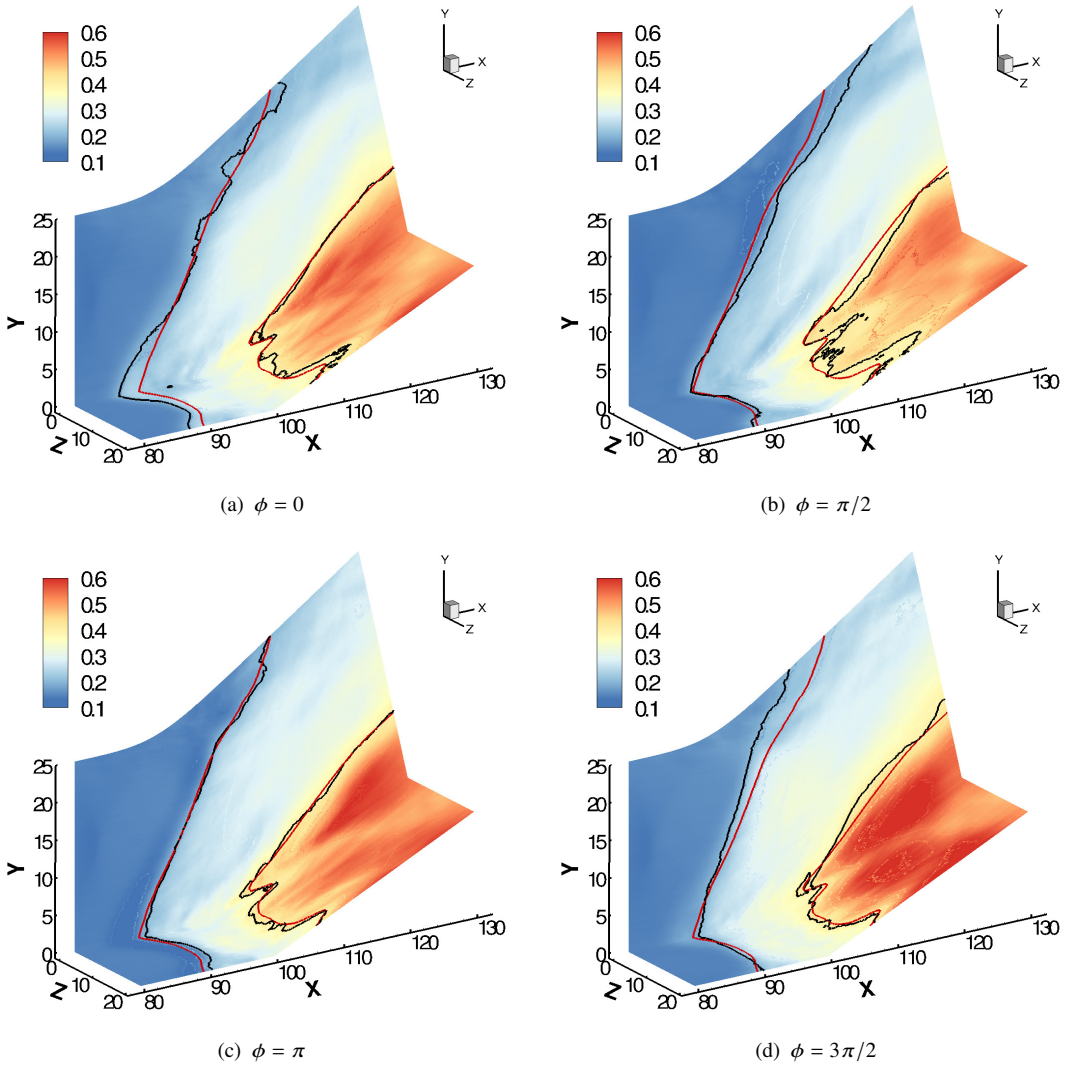

(a) $\phi = 0$ (b) $\phi = \pi/2$

(c) $\phi = \pi$ (d) $\phi = 3\pi/2$

Fig. 14 Contours of $\hat{p}/p_\infty$ depicting the low-frequency motion of the compression-ramp shock and the reattachment shock-system. Red and black solid lines represent the mean and instantaneous contour levels of $\hat{p}/p_\infty = 0.2$ and 0.4 respectively.

Initially at $\phi = 0$ in Fig. 15(a), the compression-ramp shock lies upstream of its mean location on the wall, while the reattachment shock-system lies downstream. Note the corrugated nature of the latter, wherein the extremities of the contour level (lying in the range $0 \leq Z \leq 5$ and $15 \leq Z \leq 20$) are displaced slightly downstream as compared to the contour level in the vicinity of the centerline. These extremities are most likely caused by the λ-shock structures on the sidewalls. On the left-sidewall, a portion of the compression-ramp shock close to the wall ($0 \leq Y \lessapprox 10$) lies

upstream of its mean while the rest of it lies approximately on its mean. The trace of the reattachment shock-system lies on its mean on the left-sidewall. In Fig. 15(b) at $\phi = \pi/2$, both the compression-ramp shock and the reattachment shock-system translate downstream of their respective mean locations, which is then followed by an upstream movement of the latter at $\phi = \pi$ (see Fig. 15(c)). At this phase, the compression-ramp shock remains downstream of its mean which then moves upstream at $\phi = 3\pi/2$ in Fig. 15(d). Based on these figures, there exists a finite time-delay between the oscillations of the compression-ramp shock and the reattachment shock-system. Also, note that the motion of parts of the compression-ramp shock lying above and below $Y \approx 10$ are not synchronous.

The motion of the interaction at $St = 0.12$ is shown in Fig. 14. The template used in the previous figure is reproduced here. The right-sidewall ($Z = 20$) is included as a translucent surface to visualize the motion described hereafter. For the upcoming analysis, we focus only on the motion of the compression-ramp shock.

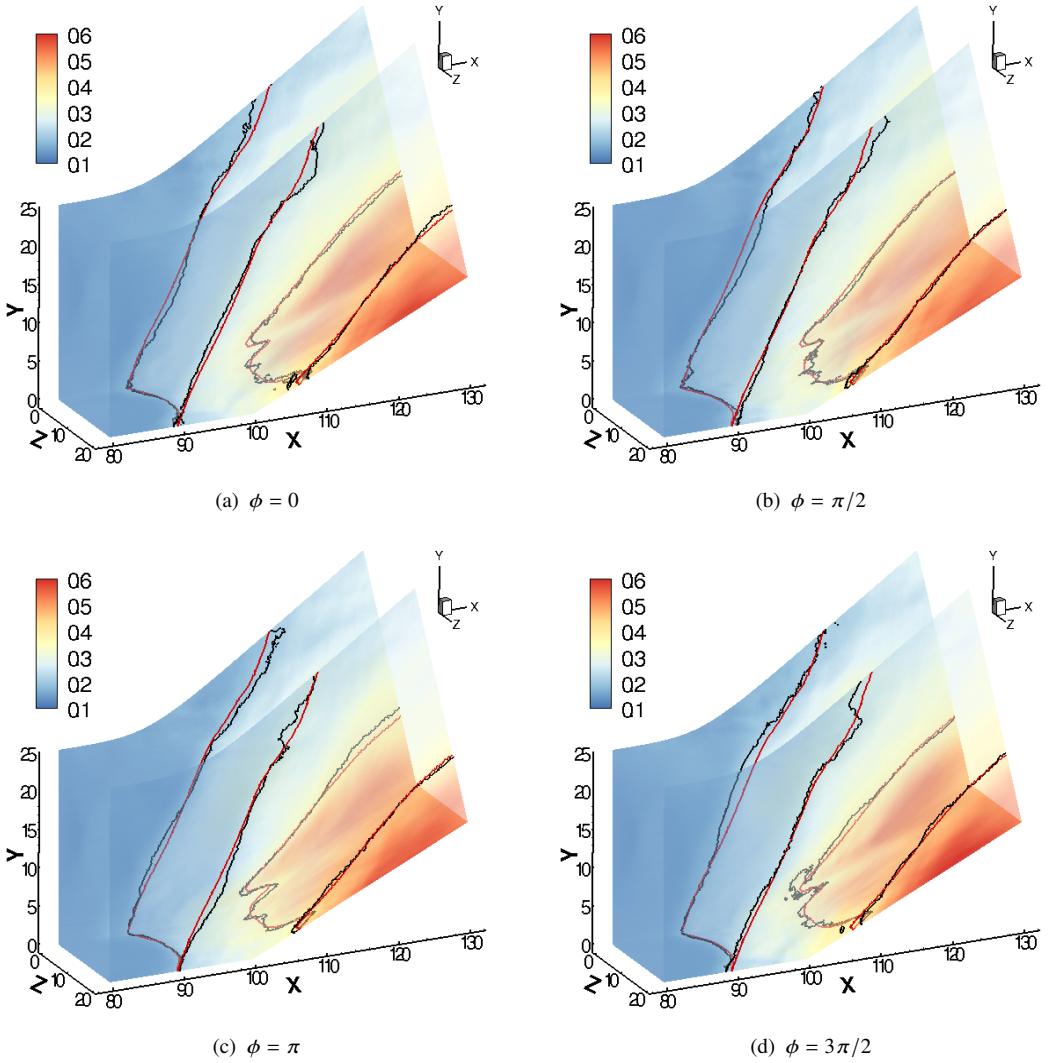

(a) $\phi = 0$ (b) $\phi = \pi/2$

(c) $\phi = \pi$ (d) $\phi = 3\pi/2$

Fig. 15 Contours of $\hat{p}/p_\infty$ depicting the low-mid frequency motion of the compression-ramp shock and the reattachment shock-system. Red and black solid lines represent the mean and instantaneous contour levels of $\hat{p}/p_\infty = 0.2$ and 0.4 respectively.

At $\phi = 0$ in Fig. 14(a), the compression-ramp shock on the left-sidewall lying in $Y \lessapprox 15$ is downstream of its mean, while the rest of it is approximately upstream of it. An opposite trend is observed on the right-sidewall at this instant. In Fig. 14(b) at $\phi = \pi/2$, the lower portions of the compression-ramp shock on the left and right-sidewall ($Y \lessapprox 5$) begin to move upstream and downstream of their respective mean locations. This is followed by their upper portions

($Y \gtrapprox 15$) moving in opposite directions at $\phi = \pi$ (see Fig. 14(c)), while the lower portions on the left and right-sidewall begin translating downstream and upstream of their mean locations. The compression-ramp shock front at $\phi = 3\pi/2$ in Fig. 14(d) returns to its original location (corresponding to $\phi = 0$), and the cycle repeats. Based on this description, the low-mid frequency mode highlights a low-amplitude asymmetric streamwise motion of the interaction. This asymmetric motion of the interaction was observed by Poggie and Porter [16] on plotting conditionally averaged wall pressure (see Figs. 16 and 17 in that reference) as well as in the coherence plots by Deshpande and Poggie [24] (see Figs. 8 and 9 in that reference). One of the contributing factors for this phenomenon could be variation in the size of the sidewall separated zones, as described in Fig. 10 on the ramp-normal plane at this frequency.

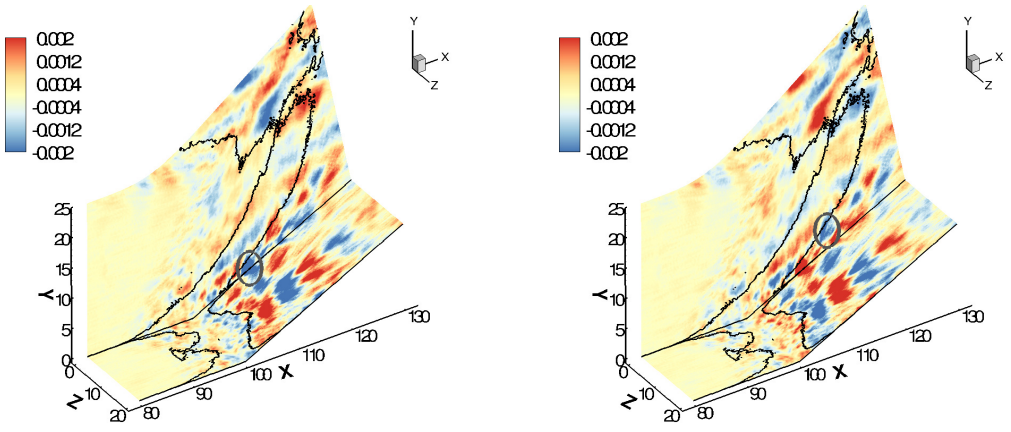

(a) $\phi = 0$ (b) $\phi = \pi$

Fig. 16 Contours of $\widehat{p'}/p_\infty$ depicting the mid-frequency vortex shedding. Black solid lines represent the mean contour level of $c_{f_x} = 0$.

Figure 16 illustrates the process of vortex shedding through contours of $\widehat{p'}/p_\infty$ for the frequency component $St = 0.6$. The reconstructed mode does not include contribution from the mean flowfield, and two instances at $\phi = 0$ and $\phi = \pi$ are shown in Figs. 16(a) and 16(b) respectively. The mean contour level of $c_{f_x} = 0$ is included as a black solid line. From both the figures, the vortices on the wall and away from the centerline are swept towards the corners and into the corner vortex system present at the sidewall junctures (see Fig. 7(b)). It seems that the sidewall vortex system transports the shed vortices from the wall to the left-sidewall, which then follow a helical trajectory of the open separation vortex. This process can be visualized by tracking the encircled region in the figure, which enters the corner vortex system associated with left-sidewall at $\phi = 0$, followed by the sidewall separation vortex at $\phi = \pi$. This observation is consistent with the behaviour of the mid-frequency mode in Sec. III.B (see Fig. 11). The vortices in the vicinity of the centerline follow the path of the core flow as shown in Fig. 6.

IV. Conclusions

Sparsity-Promoting Dynamic Mode Decomposition was performed on the data set obtained from high-fidelity computations of a highly confined SBLI. The mean flowfield on the sampled planes suggested a complex three-dimensional flowfield characterized by secondary flows. The spectral analysis presented Ref. [24] as well as Fig. 2(b) highlighted dominant time-scales in the low, low-mid, and mid-frequency band. The eigenspectrum obtained from SPDMD for all the cases indicated a statistically stationary system. Using this observation, the oscillatory part of modes corresponding to a representative frequency from each band were reconstructed and examined at different phase angles. Also, neutral DMD modes suggested that a continuous input of disturbances from the incoming turbulent flow is requried to maintain unsteadiness in this flow. This procedure highlighted several complex phenomena present in the flowfield, which were not readily evident from statistical analysis carried out by Poggie and Porter [16] and Deshpande and Poggie [24].

On the centerplane, the low-frequency mode ($St = 0.03$) highlighted separation bubble breathing coupled with the oscillations of the compression-ramp shock. The shock moved upstream in the bubble expansion phase and downstream when it contracted. The low-mid frequency mode ($St = 0.12$) showed the flapping of the shear layer which responded

to the variation in the instantaneous size of the separated zone. The mid-frequency mode indicated vortex shedding ($St = 0.6$) from the separated zone, which also affected the instantaneous reattachment location. Similar analysis on the ramp-normal plane showed in-phase breathing motion of the sidewall separated zones at low-frequency. In addition to the streamwise motion of the λ-shock feet, their spanwise motion was also affected by the aforementioned breathing motion. Asymmetric expansion and contraction of the sidewall separated zones occurred at the low-mid frequency, while the mid-frequency mode showed the spanwise transport of the vortical structures present on the wall, into the open separation vortex on the sidewalls through the corner vortex system.

The low-frequency mode on the wall and sidewalls highlighted the oscillations of the compression-ramp shock and the reattachment shock-system downstream on the ramp. These oscillations were slightly out of phase. Additionally, oscillations of the portions of the compression-ramp shock closer to the wall and in the freestream were not synchronous. Alternating streamwise motion of the interaction, possibly caused by the asymmetric expansion and contraction of the sidewall separated zones, occurred at the low-mid frequency. The mid-frequency mode showed vortex shedding from the separated region on the floor. The structures shed away from the centerline follow a pattern observed for the mid-frequency mode corresponding to the ramp-normal case, i.e. they are swept away from the midspan and into the sidewall separation vortex. Those that are shed in the vicinity of the centerline are aligned with the core flow. In this study, the domain size was reduced owing to memory constraints on a single node. Therefore for future studies, the authors plan to employ the parallel DMD algorithm formulated by Sayadi and Schmid [29]. Additionally, the issue of sensitivity of DMD to noise will be addressed by adapting the two-stage algorithm proposed by Hemati et al. [30].

Acknowledgments

This work was supported in part by the U.S. Air Force Office of Scientific Research grant FA9550-17-1-0153, monitored by I. Leyva. Computer time was provided by Purdue University's Rosen Center for Advanced Computing. The original computation was supported by the DOE INCITE Program. This research used resources of the Argonne Leadership Computing Facility, which is a DOE Office of Science User Facility supported under Contract No. DE–AC02–06CH11357.

References

[1] Green, J. E., "Interactions between shock waves and turbulent boundary layers," *Progress in Aerospace Sciences*, Vol. 11, 1970, pp. 235–340.

[2] Dolling, D. S., "Fifty years of shock-wave/boundary-layer interaction research: what next?" *AIAA Journal*, Vol. 39, No. 8, 2001, pp. 1517–1531.

[3] Gaitonde, D. V., "Progress in shock wave/boundary layer interactions," *Progress in Aerospace Sciences*, Vol. 72, 2015, pp. 80–99.

[4] Clemens, N. T., and Narayanaswamy, V., "Low-frequency unsteadiness of shock wave/turbulent boundary layer interactions," *Annual Review of Fluid Mechanics*, Vol. 46, 2014, pp. 469–492.

[5] Reda, D. C., and Murphy, J. D., "Shock wave/turbulent boundary-layer interactions in rectangular channels," *AIAA Journal*, Vol. 11, No. 2, 1973, pp. 139–140.

[6] Reda, D. C., and Murphy, J. D., "Sidewall boundary-layer influence on shock wave/turbulent boundary-layer interactions," *AIAA Journal*, Vol. 11, No. 10, 1973, pp. 1367–1368.

[7] Bruce, P. J. K., Burton, D. M. F., Titchener, N. A., and Babinsky, H., "Corner effect and separation in transonic channel flows," *Journal of Fluid Mechanics*, Vol. 679, 2011, pp. 247–262.

[8] Burton, D. M. F., and Babinsky, H., "Corner separation effects for normal shock wave/turbulent boundary layer interactions in rectangular channels," *Journal of Fluid Mechanics*, Vol. 707, 2012, pp. 287–306.

[9] Xiang, X., and Babinsky, H., "Corner effects for oblique shock wave/turbulent boundary layer interactions in rectangular channels," *Journal of Fluid Mechanics*, Vol. 862, 2019, pp. 1060–1083.

[10] Eagle, W. E., and Driscoll, J. F., "Shock wave–boundary layer interactions in rectangular inlets: three-dimensional separation topology and critical points," *Journal of Fluid Mechanics*, Vol. 756, 2014, pp. 328–353.

[11] Funderburk, M., and Narayanaswamy, V., "Experimental investigation of primary and corner shock boundary layer interactions at mild back pressure ratios," *Physics of Fluids*, Vol. 28, No. 8, 2016, 086102.

[12] Garnier, E., "Stimulated detached eddy simulation of three-dimensional shock/boundary layer interaction," *Shock waves*, Vol. 19, No. 6, 2009, p. 479.

[13] Bisek, N., "Sidewall interaction of a supersonic flow over a compression ramp," AIAA Paper 2015–1976, American Institute of Aeronautics and Astronautics, Kissimmee, FL, January 2015.

[14] Wang, B., Sandham, N. D., Hu, Z., and Liu, W., "Numerical study of oblique shock-wave/boundary-layer interaction considering sidewall effects," *Journal of Fluid Mechanics*, Vol. 767, 2015, pp. 526–561.

[15] Rabey, P. K., Jammy, S. P., Bruce, P. J. K., and Sandham, N. D., "Two-dimensional unsteadiness map of oblique shock wave/boundary layer interaction with sidewalls," *Journal of Fluid Mechanics*, Vol. 871, 2019.

[16] Poggie, J., and Porter, K. M., "Flow structure and unsteadiness in a highly confined shock-wave–boundary-layer interaction," *Physical Review of Fluids*, Vol. 4, No. 2, 2019, 024602.

[17] Schmid, P. J., "Dynamic mode decomposition of numerical and experimental data," *Journal of Fluid Mechanics*, Vol. 656, 2010, pp. 5–28.

[18] Schmid, P. J., Li, L., Juniper, M. P., and Pust, O., "Applications of the dynamic mode decomposition," *Theoretical and Computational Fluid Dynamics*, Vol. 25, No. 1–4, 2011, pp. 249–259.

[19] Grilli, M., Schmid, P. J., Hickel, S., and Adams, N. A., "Analysis of unsteady behaviour in shockwave turbulent boundary layer interaction," *Journal of Fluid Mechanics*, Vol. 700, 2012, pp. 16–28.

[20] Nichols, J. W., Larsson, J., Bernardini, M., and Pirozzoli, S., "Stability and modal analysis of shock/boundary layer interactions," *Theoretical and Computational Fluid Dynamics*, Vol. 31, No. 1, 2017, pp. 33–50.

[21] Pirozzoli, S., Larsson, J., Nichols, J., Bernardini, M., Morgan, B., and Lele, S., "Analysis of unsteady effects in shock/boundary layer interactions," *Proceedings of the Summer Program, Center for Turbulence Research*, 2010, pp. 153–164.

[22] Pasquariello, V., Hickel, S., and Adams, N. A., "Unsteady effects of strong shock-wave/boundary-layer interaction at high Reynolds number," *Journal of Fluid Mechanics*, Vol. 823, 2017, pp. 617–657.

[23] Statnikov, V., Sayadi, T., Meinke, M., Schmid, P., and Schröder, W., "Analysis of pressure perturbation sources on a generic space launcher after-body in supersonic flow using zonal turbulence modeling and dynamic mode decomposition," *Physics of Fluids*, Vol. 27, No. 1, 2015, 016103.

[24] Deshpande, A. S., and Poggie, J., "Unsteadiness of Shock-Wave/Boundary-Layer Interaction with Sidewalls," AIAA Paper 2020–0581, American Institute of Aeronautics and Astronautics, Orlando, FL, January 2020.

[25] Jovanović, M. R., Schmid, P. J., and Nichols, J. W., "Sparsity-promoting dynamic mode decomposition," *Physics of Fluids*, Vol. 26, No. 2, 2014, 024103.

[26] Poggie, J., "Effect of Forcing on a Supersonic Compression Ramp Flow," *AIAA Journal*, Vol. 57, No. 9, 2019, pp. 1–8.

[27] Eaton, J. K., and Johnston, J. P., "Low frequency unsteadyness of a reattaching turbulent shear layer," *Turbulent Shear Flows 3*, edited by L. Bradbury, F. Durst, B. E. Launder, F. W. Schmidt, and J. H. Whitelaw, Springer, New York, 1982, Chap. 3, 1st ed., pp. 162–170.

[28] Deshpande, A. S., and Poggie, J., "Flow Control of Swept Shock-Wave/Boundary-Layer Interaction Using Plasma Actuators," *Journal of Spacecraft and Rockets*, Vol. 55, No. 5, 2018, pp. 1198–1207.

[29] Sayadi, T., and Schmid, P. J., "Parallel data-driven decomposition algorithm for large-scale datasets: with application to transitional boundary layers," *Theoretical and Computational Fluid Dynamics*, Vol. 30, No. 5, 2016, pp. 415–428.

[30] Hemati, M. S., Rowley, C. W., Deem, E. A., and Cattafesta, L. N., "De-biasing the dynamic mode decomposition for applied Koopman spectral analysis of noisy datasets," *Theoretical and Computational Fluid Dynamics*, Vol. 31, No. 4, 2017, pp. 349–368.